Rings Based Zero-field-cooled YBCO Magnetic Bearing

Miguel Marques de Lima Roque
miguel.roque@tecnico.ulisboa.pt
Instituto Superior Técnico, Universidade de Lisboa, Lisboa, Portugal
October 2017

***Abstract*— This thesis focuses on improving the configuration of a superconducting bearing that works with magnetic levitation. The work developed for such purpose is described in the following paragraphs.**

The configuration of a rotor with continuous permanent magnets rather than discontinuous was developed in order to achieve a more stable and smooth rotation. The feasibility of this design was simulated and tested using an experimental prototype.

A finite element model was developed to study the energy transmission in the stator of the bearing prototype and the liquid nitrogen evaporation rate was analyzed. The results obtained in simulation and experimentally were compared. A new configuration has also been created in order to minimize this rate of evaporation.

An experimental assembly was developed to connect the bearing to an electric motor to test the rotation of the rotor in order to compare the behavior using the discontinuous rotor and new continuous rotor.

An assembly was developed to couple a high-resolution sensor in order to analyze the bearing vibrations and stability in operation.

The study of the dynamic behavior of the system axially and radially, respectively, was also performed.

The feasibility of the system using the two possible cooling techniques was analyzed: Field Cooling and Zero Field Cooling.

This work continues the previous work that allowed the successful design of a frictionless friction bearing based on superconducting technology. Superconducting bulks together with permanent magnets are nowadays used to create levitation systems, since they allow stable configurations among themselves and do not require the use of electromagnetic stabilizers. The main goal of this project is to use this technology to create a bearing for electric machines.

Keywords— Superconductor magnetic bearing; Zero Field Cooling; High temperature superconductor; Ring based permanent magnets; Magnetic levitation; Bearing for electrical machines.

I. INTRODUCTION

BEARINGS have played an important role since their invention and from the first industrial revolution the utilization of these components in mechanical systems and machines has widely increased. In the 1980s magnetic bearing systems became emerging technologies [1] and since then, mechanical bearings have been replaced by magnetic bearings in specific applications and environments. In fact, magnetic bearings reveal benefits for rotating components to work in high speed, high power and without mechanical contact or friction [2].

Regarding to frictionless bearings, new strategies using permanent magnets (PM) and type II superconductor bulks are increasingly being studied to create levitation bearings and flywheels, mainly due to the stability of this kind of systems. In [3] a passive Superconducting Magnetic Bearing (SMB) was investigated to create a more effectiveness twist element in the textile technological process of ring spinning, since frictional wear and heat are the limiting factors for productivity of such devices. A multi-surface levitation concept using three PMs and one High Temperature Superconductors (HTS) is studied for different configurations in [4], to reach the highest possible levitation forces in order to maximize the stiffness of a mechanical flywheel system. In [5] a HTS Bearing was tested using Zero-Field-Cooled (ZFC) and Field Cooling (FC). The results of both techniques were compared, concerning axial forces, axial stiffness and their characteristics. Other authors have deeply studied important features of SMB, namely dynamical stiffness models [6] and effect of the magnetic configuration on the rotational motion [7].

However, most of studied levitation systems use the FC to cool the HTSs. The ZFC reveals some advantages, when compared with the field cooling technique, because FC implies significant hysteresis losses due to the magnetic flux trapping [8]. In previous works, the authors achieved reliable results using superconductor technology to study and create levitation systems, namely a new Maglev design using ZFC Yttrium Barium Copper Oxide (YBCO) superconductors [9][10], among others. Following similar concepts and strategies, a ZFC YBCO Magnetic Bearing has being developed [8][11][12]. Furthermore, for horizontal SMB, previous studies showed that Zero Field Cooling provides effective lateral stability and higher levitation forces than the commonly used FC [12]. Basing on such principles, an original ZFC-SMB was then projected and produced.

The ZFC SMB is composed by a fixed part and a rotating but levitating part, respectively stator and rotor, as shown in Fig. 1 (a) and Fig. 1 (b). The stator contains two discontinuous rings of sixteen equally spaced bulk YBCO superconductors presented in Fig. 1 (b). The rotor part contains three discontinuous rings with five equally spaced NdFeB PMs each

one. Each PM ($B_r = 1.25T$) has rectangular form with 25x25x12 mm. The three inner discontinuous rings of PMs are magnetized in alternate North-South-North way, such as the two border rings of magnets have concordant polarizations and the middle ring of magnets opposite polarization [8]. See [8] and [11] for further information.

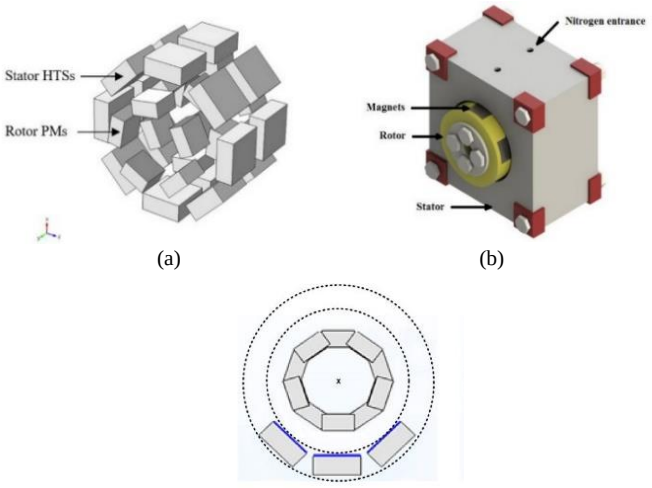

(a) (b)

(c)

Fig. 1. Project of ZFC-SMB: spatial distribution of PMs and HTSs bulks (a), final assembly (b) and YBCO bulks disposition in the real prototype stator (c).

Due to budget limitations, only six superconductors were used on the bottom of the stator in the prototype version. A representative drawback of the superconductor bulks position is shown in Fig. 1(c). Simulations and experimental tests show that the rotor and stator with such design present discontinuities that cause asymmetries on the rotation and several stable and instable angles that prevent the SMB to rotate smoothly.

In this thesis, the discontinuous PMs used previously are replaced by three NdFeB radially magnetized ring PMs with grade N40 ($B_r = 1.25T$). These magnets have similar features, when compared with the previously layout of the PMs. However, due to manufacturing limitations, there are some differences. The outer diameter is 79 mm instead of 83 mm, whilst the inner diameter is 55 mm instead of 59 mm. The main concern was to keep the thickness of 12 mm. The width remains 25 mm as well. The weight of the three rings together is 14.715 N. It is pretended the SMB design to be inherently stable with a continuous behavior. Thus, a setup was developed to connect the bearing to an electric motor to test the rotation of the rotor in order to compare the behavior using the discontinuous rotor and new continuous rotor. The conception and modelling of the new rotor is presented and the improvements and developments of the ZFC-SMB are analyzed. The viability of the prototype using FC is also addressed. Moreover, a Finite Elements Method (FEM) model was created to evaluate the energy transfer in the SMB stator to predict the system temperatures and to create a new configuration to reduce the liquid nitrogen evaporation rate.

II. Modelling

The detailed geometry and dimensions of the new SMB design based on ring PMs are shown in Fig. 2.

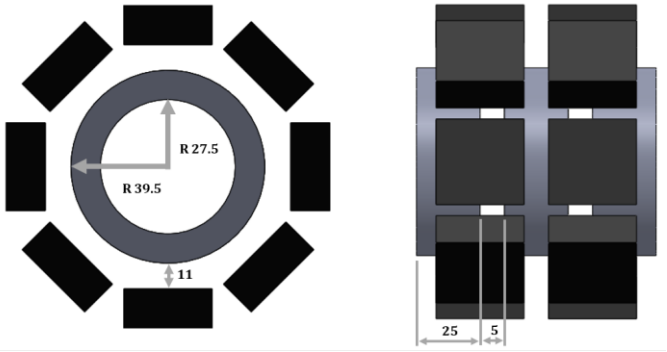

Fig. 2. Geometry and dimensions of the new SMB design for rotor D5.

The three ring PMs are magnetized in alternate North-South-North way. The distance between each ring defines the type of rotor and it is important, since Levitation and guidance forces vary with it. Three different rotors are studied: D5, D10 and D20, which means 5, 10 or 20 mm of distance between each PM. Fig. 2 represents the rotor D5.

A. Simulation of the Magnetic Flux densities

Fig. 3 and Fig. 4 represent simulated magnetic flux density involved in the SMB with six YBCO bulks in stator and ring PMs in rotor.

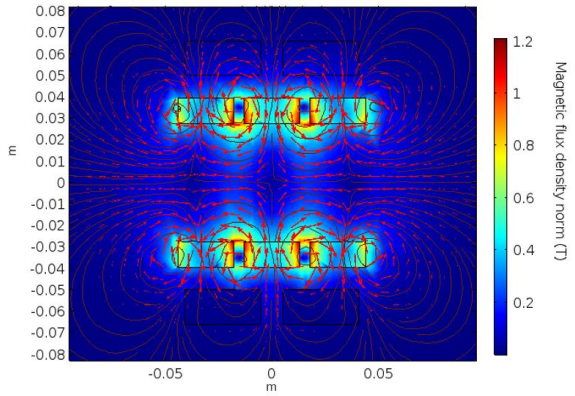

Fig. 3. Simulation of involved magnetic flux densities with rotor D5 – longitudinal view.

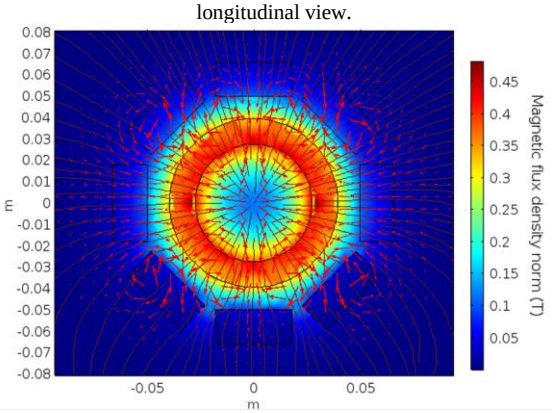

Fig. 4. Simulation of involved magnetic flux densities with rotor D5 – transversal view.

For the calculations the model presented in [8] was followed. The radial component of magnetic induction reduces in the direction of the six YBCO bulks under the rotor, because they present a relative permeability of 0.2.

B. *Prediction of Levitation and Guidance Forces*

Fig. 5 shows Levitation forces vs. rotor eccentricity obtained from the 3D Finite Element Method model, for the three different rotors. Results were obtained decentering the rotors between a range of ±7 mm, which represents the maximum radial displacement of the rotor inside the stator, keeping the safety margin of 4 mm.

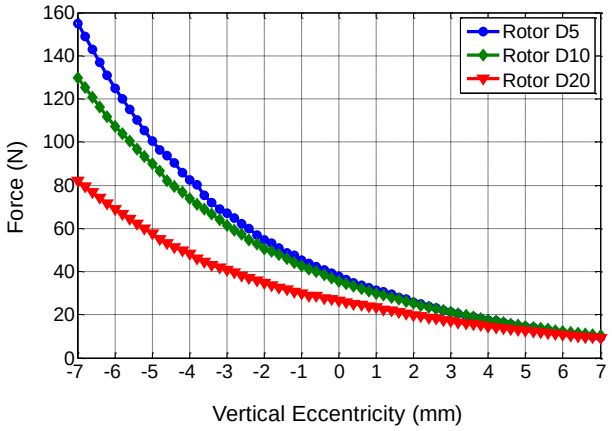

Fig. 5. Levitation rotor forces for different rotor eccentricity values. Results for the three different rotors are shown.

On the other hand, guidance forces are shown in Fig. 6. Displacement zero represents the stable position, whose rotor is centered and does not have forces applied.

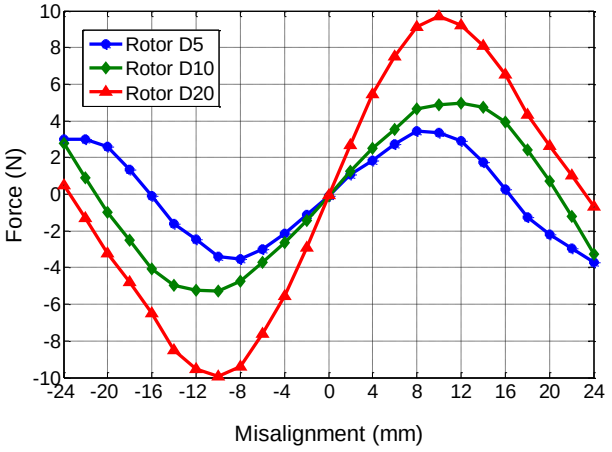

Fig. 6. Guidance rotor forces for different lateral misalignment. Results for the three different rotors are shown.

Fig. 5 and Table I show that any of the three rotors is able to sustain the total weight of the PMs, because the Levitation force with centered rotor is always higher than the rotor weight (14.715 N). Guidance forces are shown in Fig 6 and Table I.

TABLE I
LEVITATION AND GUIDANCE FORCES FOR DIFFERENT ROTORS

Rotor type	Levitation Force Centered Rotor	Maximum Guidance forces
D5	36.898 N	3.5341 N
D10	34.786 N	5.268 N
D20	26.529 N	9.7168 N

III. PROTOTYPE DESIGN

The SMB stator was not modified. All the changes in the prototype are present in the SMB rotor. A 3D CAD design was again used for its conception. See [11] and [12] for more detailed information about the SMB stator.

The rotor must reveal circular geometry and it has to support the three ring PMs as presented in Fig. 2. Further requirements are: i) keep the distances between each ring PM and between HTSs and PMs (air-gap); ii) allow an easy and practical assembly and disassembly, in such a way that the PMs damage risks are as minimum as possible; iii) be as light as possible, ensuring the stiffness of the structure; iv) develop a modular prototype.

Four main parts were designed to fulfil the requirements of the structure: two internals to keep the pretended distances between each PM and two externals. Three threaded rods are used to maintain the structure compact and six nuts are used to assemble the rotor together.

The final assembly is shown in Fig. 7, Fig. 8 and Fig. 9.

Fig. 7. Rotor exploded view.

Fig. 8. Rotor final assembly.

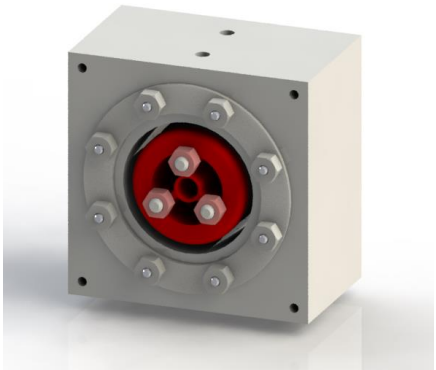

Fig. 9. SMB final assembly.

The real prototype was built up using a 3D printer. The chosen materials have relative magnetic permeability of about 1. The rotor slices and the nuts are made of Polylactic Acid (PLA) in order to have high resistance and good finishing, whilst Teflon (polytetrafluoroethylene) was used for the rods, to ensure better finishing after machining the threads. The dismounted assembly of rotor D20 is shown in Fig. 10, whilst Fig. 11 shows the D5 and D20 PM rotor prototypes. The real prototype of the rotor D5 and the stator are presented in Fig. 12.

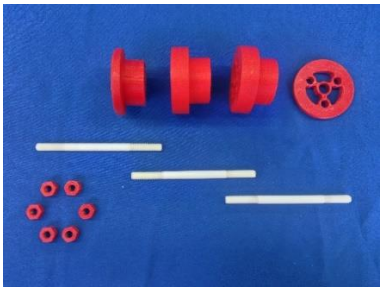

Fig. 10. Rotor D20 components.

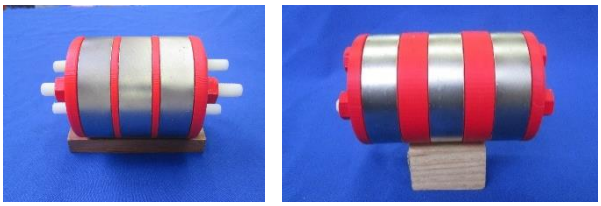

(a) Rotor D5 (b) Rotor D20

Fig. 11. SMB final assembly.

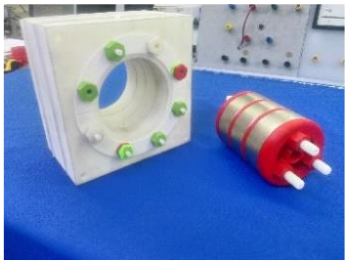

Fig. 12. Real prototype – rotor D5.

The measured weight of the rotor D5 and D20 is 15.402 N and 15.892 N, respectively.

Several tests were made to prove the stiffness of the structure and the easiness and security to mount and dismount the assembly.

IV. Measurement of Levitation and Guidance Forces

A. *Zero Field Cooling*

All the tests were made cooling the YBCO bulks in absence of magnetic field, i.e. following the ZFC technique.

Fig. 13 (a) shows the experimental setup used to measure levitating forces. The rotor levitates and the Levitation force is measured by a force sensor.

Fig. 13 (b) shows the experimental setup used to measure guidance forces. The stator is laid upon a small car, whilst the rotor remains fixed centered in the stator. An axial stator misalignment is forced pulling the car in both directions, to measure the guidance forces that push or pull the rotor to its axial equilibrium position.

(a) (b)

Fig. 13. Experimental setups to measure: a) Levitation forces, b) guidance forces.

Fig. 14 and Fig. 15 compare respectively the values of Levitation and guidance forces for rotors D5 and D20, obtained by experimental measurement and by FEM simulation.

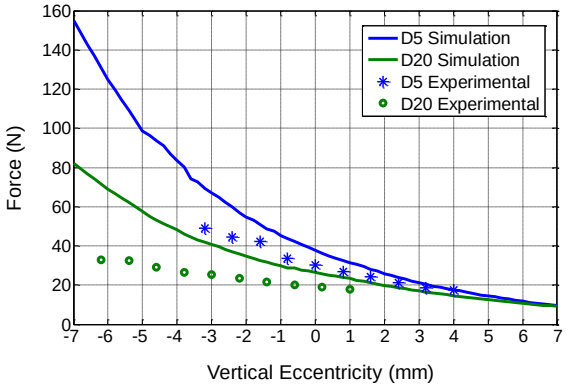

Fig. 14. Rotor Levitation forces versus vertical eccentricity.

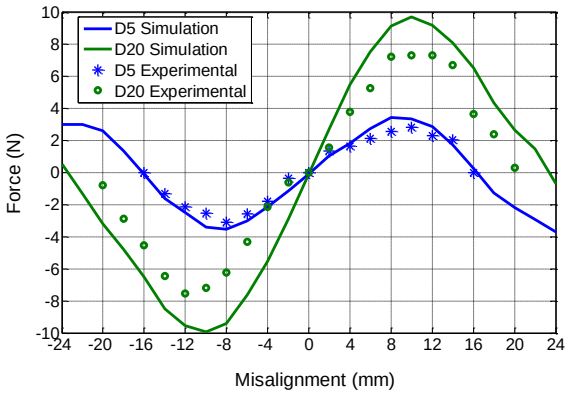

Fig. 15. Rotor guidance forces versus lateral misalignment.

The measured Levitation forces are slightly lower than the estimated in the simulations. This may be explained by the simplifications used in the theoretical model of Chapter II. Comparing with the result obtained in [11] with the discontinuous PM rotor, the levitation force is in general higher, compensating the higher weight of the continuous PM rotor.

The measured Guidance forces are close to the simulated ones for rotor D5. For rotor D20 the forces are lower than predicted. However, the inflexion points are consistent.

Table II compares the SMB force values using the old discontinuous PM rotor studied in [11] and the new continuous PM rotor using PM rings. Simulations and experimental values of Levitation and Guidance forces are presented.

TABLE II
FORCES FOR DISCONTINUOUS AND CONTINUOUS PM ROTORS D5

	Sustain Force (Centered)		Max. Guidance Forces	
Rotor D5	Simulation	Experimental	Simulation	Experimental
Disc. PM	26.91 N	18.97 N (*)	3.12 N	2.16 N
Cont. PM	37.62 N	30.26 N	3.43 N	3.10 N
Diff. (%)	139.8%	159.5%	109.9 %	143.5 %

(*) There are no data for null eccentricity in this case. The closest displacement of 0.25mm from the null eccentricity was used instead.

In all cases, the forces have increased using the new rotor. The continuous rings outperformed the discontinuous rings as expected.

B. *Field Cooling*

The viability of the prototype using FC was tested. For such purpose in the following section, an analysis of the differences in terms of forces using both cooling techniques is discussed. Notice that the SMB was conceived to work with ZFC, therefore it is expected that, using the FC procedure, the SMB is not viable. Fig. 16 shows the cooling method used.

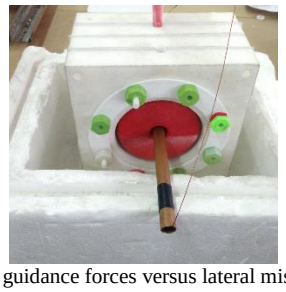

Fig. 16. Rotor guidance forces versus lateral misalignment.

Similar setups for forces measurement with ZFC were followed. Fig. 17 compares results for FC and ZFC using the same rotor. Moreover, the weight of the rotor is plotted, in order to compare with the observed forces.

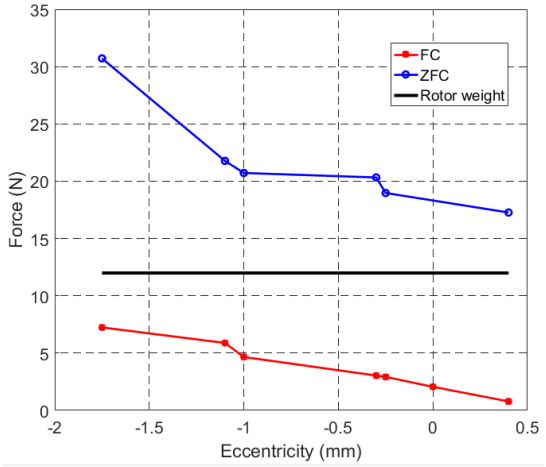

Fig. 17. Rotor guidance forces versus lateral misalignment.

As observed, the Levitation Force using FC never outperforms the rotor weight, existing no conditions for levitation.

Fig. 18 compares results for Guidance Forces using FC and ZFC. Despite the range of measured displacements for FC is not as big as the ones measured for ZFC, it is possible to conclude that the Guidance forces for FC are quite higher than the observed with ZFC.

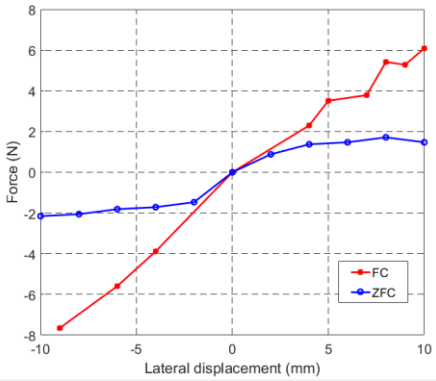

Fig. 18. Rotor guidance forces versus lateral misalignment.

Analysing both tests, it is possible to conclude that the SMB is not viable using the FC technique, because the Levitation forces are not enough to support the rotor weight. However, the Guidance forces were substantially higher. A SMB conceived to work with FC could havebetter lateral stability.

V. SMB AS BEARING FOR ELECTRICAL MACHINES - SETUP

A setup was created to evaluate the SMB behaviour operating as a real bearing. The main objective is to replace a mechanical bearing from an electrical machine, in order to understand if the SMB sustains the weight of the system and rotates in a stable way.

The setup must include an electrical motor and the SMB, besides a shaft to link both components. Fig. 19 shows the first proposal of the setup. Table III explains the further components and them functions.

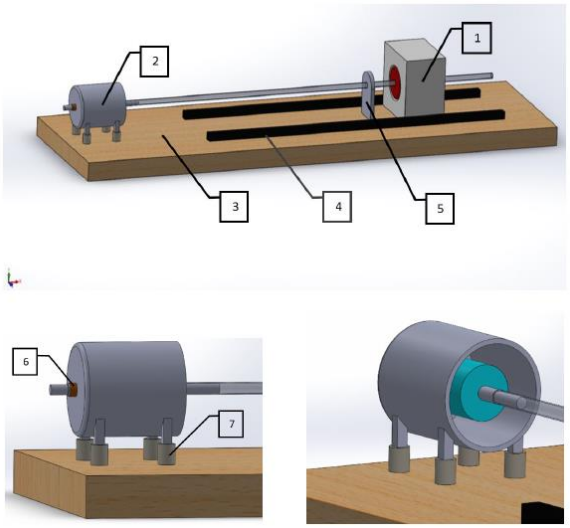

Fig. 19. Outline projected.

TABLE III
OUTLINE COMPONENTS

Number	Designation	Function
1	SMB (discont. PM rotor D5)	-
2	Eletric Motor	-
3	Wooden Board	To support and fix all the components
4	-	To avoid the movement of the SMB (longitudinal)
5	Protector	To protect the stator from possible oscillations and/or misalignments
6	Shaft axial holder	To avoid the motor's rotor to come out from the stator
7	Supports	To elevate the motor to align it with the SMB

Fig. 20 shows the components projected and the whole system. There are some small differences, when compared with the first outline. However, the requirements are fulfilled.

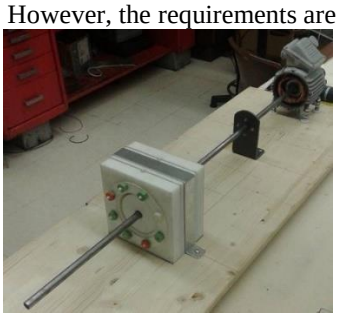

Fig. 20. Components and setup before the experiments.

Furthermore, an Altivar 31 frequency inverter was set to allow soft starts of the motor and to control the angular speed of the motor.

However, it was not possible to start the motor in such conditions. After remove one of the mechanical bearing, the rotor does not rotate and it is blocked instead. Several approaches were tried to solve the problem, namely the construction of a new motor's rotor and the change of an one-phase electrical machine to a three-phases one. Fig. 20 shows the original motor's rotor (above), with diameter of 55.5 mm, and the constructed for this setup (below), with 50 mm.

Fig. 21. Old and new motor's rotor.

A high resolution fibreoptic sensor PHILTEC, Inc. RC190 was set pointed to the shaft, in order to evaluate vibrations in the system operating. The final setup can be observed in Fig.22.

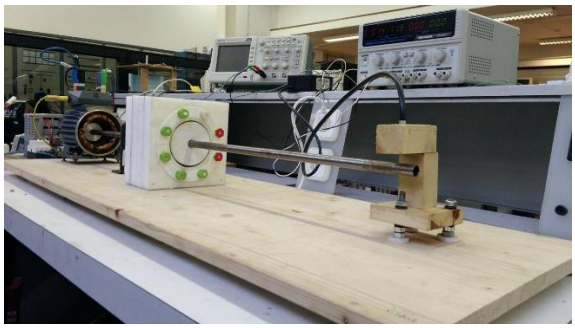

Fig. 22. Final setup.

VI. Dynamic Tests

Besides the static analysis made in previous section, dynamic analysis is required to understand the viability of the SMB operating, i.e., to understand how the system behaves rotating. Thus, the experimental setup of Chapter V was installed, on one hand to test the SMB as a bearing for electrical machines and on other hand to compare the stability and the smoothness between the operation of the SMB using discontinuous PMs [8][11][12] and the SMB using the new continuous PM rings. The system speed was measured through a digital tachometer RS 163-5348. To evaluate stability, a current probe was set to analyse the supply current

A. *Analysis of vibrations of the motor shaft*

Fig. 23 shows the vibrations evaluation experiment.

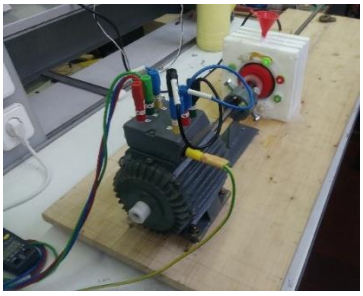

Fig. 23. Evaluating vibrations.

Table IV shows the fundamental frequencies of the supply current from the inverter and measured by the displacement sensor, for several rotor angular speeds tested. In this table, f_R is the rotor frequency of rotation measured by a tachometer, f_{S1} the fundamental frequency of the signal from the displacement sensor and f_{C1} the fundamental frequency of the supply current from the inverter. This table shows also the operating slip s, calculated according to expression (1)

$$S = \frac{f_{C1} - p\, f_R}{f_{C1}} \quad (1)$$

where $p = 2$ is the driving motor number of dipoles.

TABLE IV
VIBRATIONS FOR SEVERAL ROTOR SPEEDS TESTED

Rotor D5	$f_R\,(Hz) = \frac{RPM}{60}$	Sensor $f_{S1}\,(Hz)$	Current $f_{C1}\,(Hz)$	Slip $s\,(\%)$
Discontinuous PM rotor	9.17 Hz (550 rpm)	6.16	47	61
	13.2 Hz (820 rpm)	11.96	50	47.2
Continuous PM rotor	4.17 Hz (250 rpm)	4.39	17	50.9
	8.33 Hz (500 rpm)	7.64	25	33.4
	15 Hz (900 rpm)	14.61	40	25

For all the tested rotor speeds, the spectrum of the signal from the displacement sensor consists on a series of frequency harmonics multiple of the fundamental frequency harmonic at f_{S1}, that is almost the same as the rotor angular frequency. This corresponds in time to a series of thin pulses with period $T_S = 1/f_{S1}$. This kind of spectrum is generally associated with mechanical looseness in electrical motors [13] and it is observed when the bearings of the machine are not properly fixed, i.e., when there is free space between the bearing and the bearing support.

Fig. 24 show the spectrum from the supply current signal for the discontinuous rotor operating a 550 rpm.

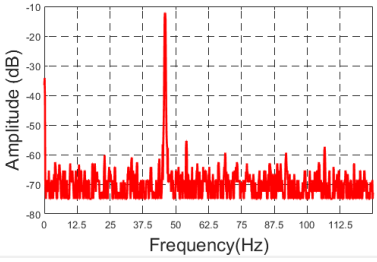

Fig. 24. Displacement supply current spectrum, for disconti. rotor at 550 rpm.

Fig. 25 and Fig. 26 show the spectrum from the displacement sensor signal, for the discontinuous PM rotor and continuous PM rotor operating at an angular speed of 550 rpm and 500 rpm, respectively. Fig. 27 and Fig. 28 show the same spectrum, for the discontinuous PM rotor and continuous PM rotor operating at an angular speed of 820 rpm and 900 rpm, respectively.

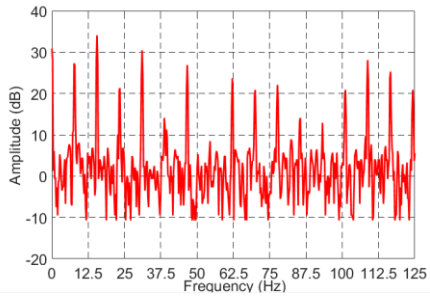

Fig. 25. Displacement sensor spectrum, for continuous rotor at 500 rpm.

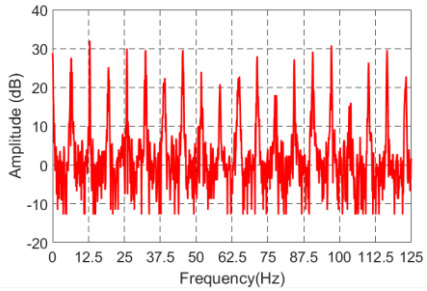

Fig. 26. Displacement sensor spectrum, for discontinuous rotor at 550 rpm.

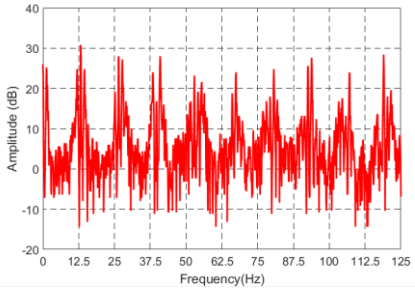

Fig. 27. Displacement sensor spectrum, for discontinuous rotor at 820 rpm.

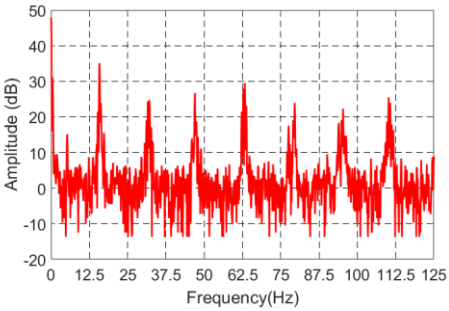

Fig. 28. Displacement sensor spectrum, for continuous rotor at 900 rpm.

For rotor speeds close to 500 rpm, Fig. 25 and Fig. 26 show that the number and amplitude of harmonics from displacement rotor spectrum are generally higher for the discontinuous PM rotor. This suggests that the vibrations are higher for discontinuous PM rotor for speeds around 500 rpm.

On the other hand, for speeds close to 900 rpm (Fig. 27 and Fig. 28) the difference in the number of harmonics and their amplitude, observed between the discontinuous and continuous PM rotor, was attenuated (when compared with speeds close to 500 rpm) and they are approximately the same for both rotors. Hence, it is possible to conclude that the biggest difference, between the discontinuous and continuous PM rotor in terms of oscillations, is the operation in lower angular velocities. The fact that the discontinuous rotor was not able to operate at speeds below 300 rpm, enhances this idea.

By analysing the slips, it is noticeable that for the most of the performed tests the values are high, almost nonsensical in a normal electrical machine. However, it is known that the electrical motor was modified and with the experiments conditions, the motor's air-gap was increased. Such conditions lead to an augmentation of the operation slip. Nevertheless, the slip values can give useful information. Comparing the results of table IV, it is observable that the slip associated to the continuous rotor is lower than one verified with the discontinuous rotor. Thus, it is observable that the unstable rotation of the discontinuous PM rotor lead to highest slip values, because the existing torque oscillations due to the intermittent rotation of the discontinuous PM ring works as an extra load torque for the motor.

Moreover, it is noticeable that increasing the angular speed, the slip values decreases for both rotors. At 1350 rpm the continuous PM rotor presented a slip value of 10%, which is the value of the three-phase motor slip before the modifications. From table III, the operating slip values for similar rotor speeds are higher with the discontinuous PM rotor, meaning that the resistive torque of this rotor is higher than for the continuous PM rotor.

B. Radial dynamics

Fig. 29 shows the setup used to evaluate the radial dynamics of the system. The displacements are measured in the shaft coupled to the rotor and pulled in the opposite direction of the sensor onto the position where the rotor touches the stator, which is around 7 mm. The shaft is again dropped off and the displacement measured throughout the time.

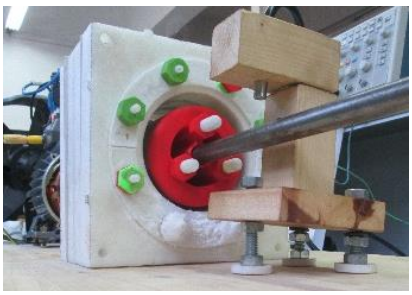

Fig. 29. Experimental setup used to evaluate the radial dynamics.

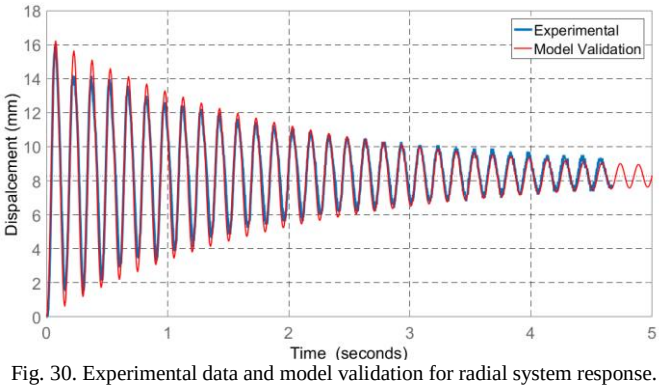

Fig. 30. Experimental data and model validation for radial system response.

Fig. 30 shows the displacement of the rotor after conversion and the validation of the model.

The radial dynamics of the system is modelled with a fit level of 83.91%, by the transfer function (2)

$$G_r(s) = \frac{1811}{s^2 + 1.019s + 1746} \quad (2)$$

that defines a 2nd-order system.

C. Axial dynamics

Fig. 31 shows the setup used to acquire the system step response. The stator is 10 mm pulled from the stable position and dropped off. The position throughout the time is measured by a position sensor.

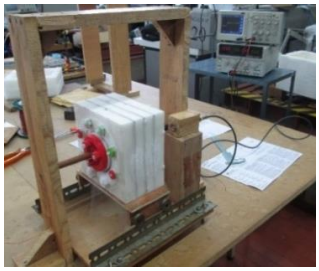

Fig. 31. Experimental setup used to acquire the axial dynamics.

Fig. 32 shows the obtained responses curve and the simulations of the model response.

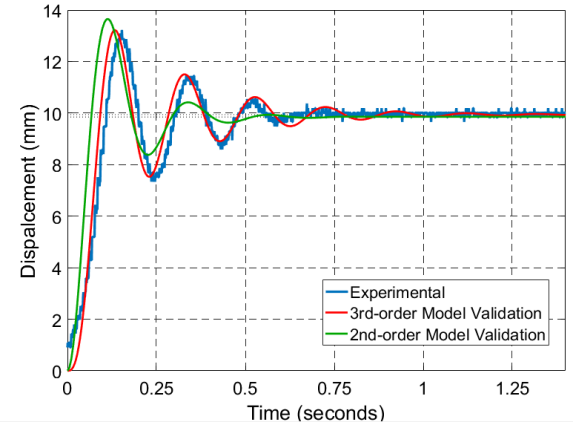

Fig. 32. Experimental data and model validation for axial system response.

The axial dynamics of the system is modeled with a fit level of 70.32% by the transfer function presented in (3)

$$G_a(s) = \frac{830.7}{s^2 + 16.81s + 843.5} \quad (3)$$

that defines a 2nd-order system and with a fit level of 88.49% by the transfer function presented in (4)

$$G_a(s) = \frac{3.47\times10^4}{s^3 + 41.06s^2 + 1365s + 3.495\times10^4} \quad (4)$$

that defines a 3rd-order system.

VII. Temperature and Heat Transfer Analysis

The thermal analysis of the component full of liquid nitrogen requires, besides the temperatures of the environment and the liquid nitrogen, the convection coefficient, *h*. To find this coefficient two different surfaces of the stator were considered. Fig. 33 shows the two surfaces, whose *h* is considered as equal, respectively.

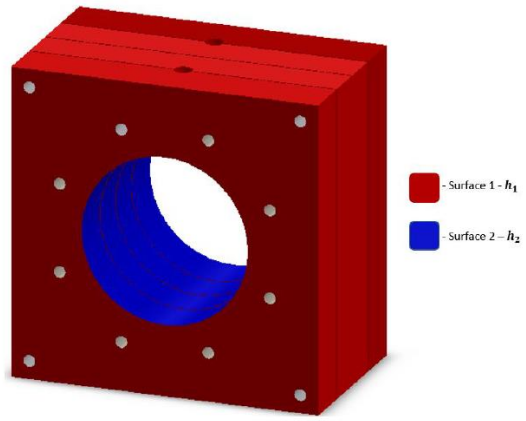

Fig. 33. Surfaces with the same *h*.

To find the film temperature, T_f, and h the temperature of both surface was measured using a thermometer CENTER 306 with measurement range from -200 ºC to 1370 ºC and resolution of 0.1 ºC. $T_1 \approx 0\,^{\circ}C = 273\ K$ and $T_2 \approx -90^{\circ}C = 235\ K$. The room temperature was considered $T_\infty = 15$ºC $= 288.15$ K. Table V shows the thermophysical properties [14] of air at the film Temperature, $T_f = \frac{T_S + T_\infty}{2}$.

TABLE V
Thermophysical Properties of Gases at Atmospheric Temp. [14]

Surface	1	2
T_f	280 K	235 K
Heat conductance, k	24.7×10^{-3} W/(m K)	21.2×10^{-3} W/(m K)
Kinematic viscosity, υ	14.11×10^{-6} m²/s	10.25×10^{-6} m²/s
Prandtl number, Pr	0.717	0.725
Thermal diffusivity, α	19.7×10^{-6} m²/s	14.2×10^{-6} m²/s
Expansion coefficient, β	3.6×10^{-3}/K	

To calculate h_1 and h_2, surface 1 is going to be approximated to a Vertical Plate with height, *L*, of 0.170 m and surface 2 as a Long Horizontal Cylinder with diameter, *D*, of 0.092 m, as explained in [14] for exercises of free convection. Hence, the Rayleigh numbers, *Ra*, are given by

$$Ra_L = \frac{g\beta_1(T_{s1} - T_\infty)L^3}{\alpha_1\upsilon_1} = 9.36\times10^6 \quad (5)$$

$$Ra_D = \frac{g\beta_2(T_{s2} - T_\infty)D^3}{\alpha_2\upsilon_2} = 1.16\times10^7 \quad (6)$$

where *g* is the gravitational acceleration. Both results show that $Ra < 10^9$, hence there is no transition to turbulent regime. The Nusselt number, *Nu*, can be then calculated by

$$\overline{Nu}_L = 0.68 + \frac{0.67Ra_L^{1/4}}{\left[1 + (0.492/\mathrm{Pr}_1)^{9/16}\right]^{4/9}} = 29.15 \quad (7)$$

$$\overline{Nu}_D = \left[0.6 + \frac{0.387Ra_D^{1/6}}{\left[1 + (0.492/\mathrm{Pr}_2)^{9/16}\right]^{8/27}}\right]^2 = 29.84 \quad (8)$$

Finally, it is possible to obtain the values of convection coefficient using

$$h_1 = \frac{\overline{Nu}_L \cdot k_1}{L} = 4.24 \text{ W / (m}^2\text{ K)} \quad (9)$$

$$h_2 = \frac{\overline{Nu}_D \cdot k_2}{D} = 6.87 \text{ W / (m}^2\text{ K)} \quad (10)$$

Using a FEM software, a model was created to thermally analyse the stator. A mesh with 10.3 mm per element was used in the simulations.

A. *Existing Stator analysis*

The simulated temperatures can be observed in Fig. 34 and Fig. 35.

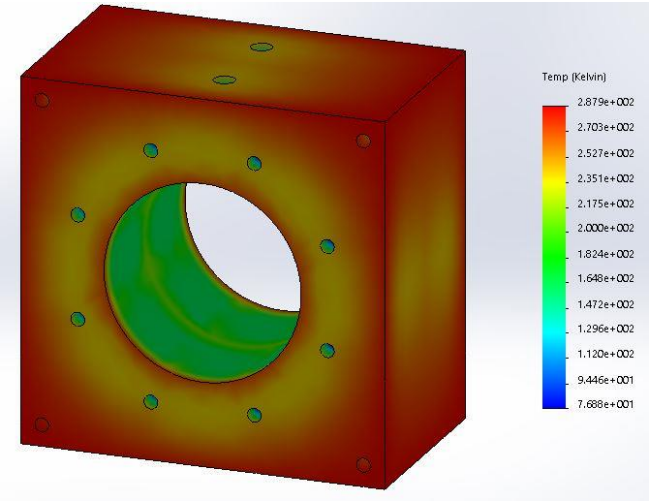

Fig. 34. Predicted external temperature.

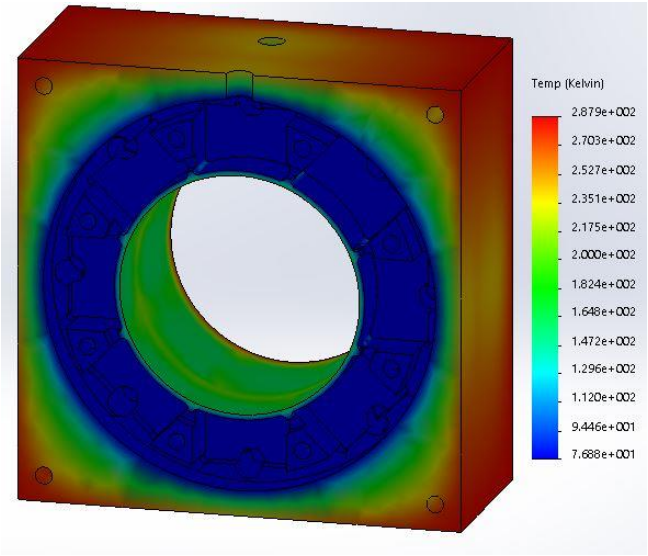

Fig. 35. Predicted internal temperature.

Based on the FEM simulation, the rate of heat transfer is q=37.445 W. The input energy required to change the state from liquid to vapour at constant temperature is called the latent heat of vaporization. The liquid nitrogen latent heat of vaporization, h_e, is 199 kJ/kg at atmospheric pressure [14]. The evaporation rate of the liquid nitrogen is calculated by

$$\frac{\partial m}{\partial t} = \frac{q}{h_e} = \frac{37.445}{199\times10^3} = 0.000188 \text{ kg/s} = 11.29 \text{ g/min} \quad (11)$$

which is 14.4 % (error percentage) higher than the values measured by the experiments. In fact, the value of liquid nitrogen vaporization rate measured in [15] was 9.67 g/min. The error may be related with the two upper holes used to refill the stator, that were not considered in the simulations and/or by the simplifications used throughout the exercise.

B. *Stator 2.0 analysis*

Notice that, analysing the model developed before, the lowest external temperature was obtained in surface 2 (Fig. 30). Hence, it is also this surface which presents the highest heat flux, since it also presents the highest thermal gradient.

Therefore, a stator with a thickness of 4 mm in walls of surface 2 was modelled and analysed thermally, in order to realize if the improvements are significant in terms of thermal isolation and liquid nitrogen evaporation rate reduction. The same convection coefficient, h_2 was used as simplification.

The results of the energy transferred with thickness in surface 2 of 2 mm with 4 mm are presented in Fig. 36 and Fig. 37, respectively.

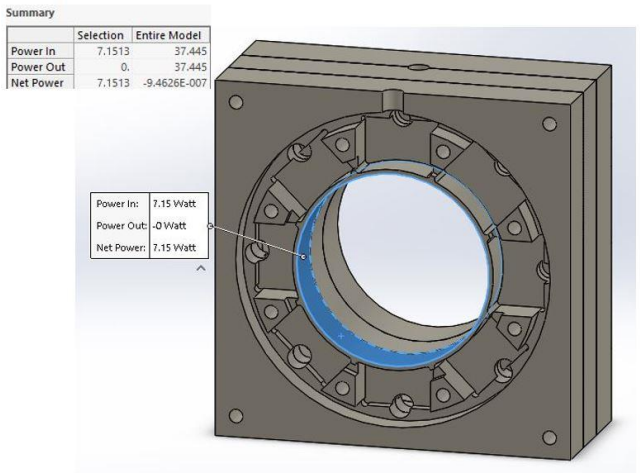

Fig. 36. Total stator heat flux with surface 2 with 2 mm of thickness.

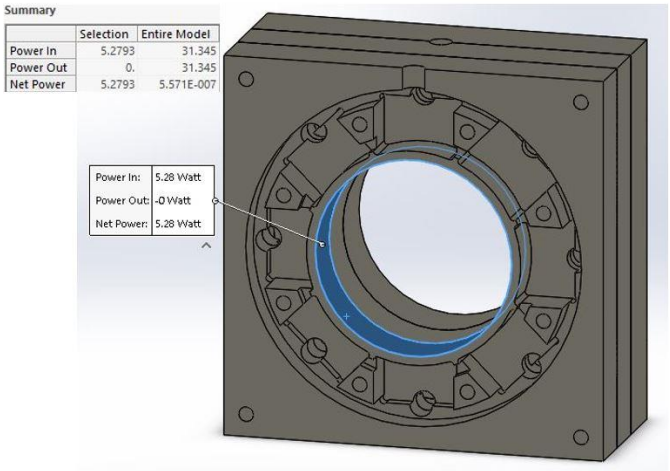

Fig. 37. Total stator heat flux with surface 2 with 4 mm of thickness.

By analysing the result, it is possible to conclude that the heat flux rates of the selected section represented in blue (Fig. 36 and Fig. 37) and the whole system decrease from 7.15 W to 5.28 W and from 37.445 W to 31.445 W, respectively. According to the simulation, the liquid nitrogen evaporation rate, calculated the same way as previously, would decrease from 11.29 g/min to 9.45 g/min in the simulated values, which corresponds to a decrease of 16.3 %. Thus, a noticeable improvement in the isolation of the structure would be achieved by the new configuration.

VIII. Conclusion

In this thesis, a new improved configuration for the horizontal SMB based on ZFC technology was developed. For such purpose, several tools were used to analyse important features, in order to understand the best way to improve them.

A thermal model of the SMB's stator was created to analyse a possible configuration to improve the liquid nitrogen thermal isolation. Trough this model the rate of nitrogen evaporation was predicted. Temperatures and the evaporation rate simulated make are close from the measured experimentally, which validates the model. Furthermore, a new configuration of the SMB's stator was created, in order to decrease the evaporation rate.

A new design of the SMB's rotor was developed, in order to improve its rotation. In fact, using the new rotor based on continuous PMs, the observed equilibrium in the SMB is not obtained in specific angles anymore and the rotor reveals a smooth angular motion instead. Furthermore, using a setup created in this work, the behaviour analysis of the SMB operating as a bearing for electrical machines, concluded that the rotor based on ring PMs reveals advantages, in terms of vibration and slip. Thus, the SMB operating as a real bearing with the new rotor reveals more safety and efficient than the used previously.

A static study of the system was made. Generally, the Levitation and Guidance forces increase using the new rotor, despite its smaller diameter, which allows a more safety configuration for the SMB. The results of simulations and the experiments were approximated. Moreover, it was concluded that adapting the distance between PMs, the SMB can have higher Levitation force or higher lateral stability, according to the requirements.

The dynamics behaviour of the system was also studied, with the focus on the development of a active stabilizer. Notice that using sixteen HTS bulks, instead of six used in the present prototype, the dynamics could change, mainly the radial dynamics.

Finally, the viability of the SMB using FC instead of ZFC was studied. The conclusion was that the SMB is not able to operate with the use of the FC technique. However, the Guidance forces have clearly increased.

In general, noticeable advances were achieved by the SMB prototype in order to use it as a viable bearing for electrical machines. Several analyses were made successfully to prove it.

Acknowledgment

This work was supported by the FCT (Foundation for Science and Technology), through IDMEC, under LAETA, through projects UID/EMS/50022/2013 and PTDC/EEEI-EEL/4693/2014–HTSISTELEC, and by FCT fellowship SFRH/BD/117921/2016 granted to António J. Arsénio as a PhD student at the electrical engineering department in Instituto Superior Técnico and as a researcher in the R&D Institute LAETA/IDMEC.

The authors like to thank Fablab EDP and Mitera for building the stator cryostat made of high density rigid polyurethane.

References

[1] G. Bitterly, "Flywheel technology: past, present, and 21st century projections." *IEEE Aerospace and Electronic Systems Magazine* 13.8 (1998): 13-16.

[2] C. Tshizubu, J.A. Santisteban, "A simple PID controller for a magnetic bearing with four poles and interconnected magnetic flux." *Advanced Control of Industrial Processes (AdCONIP), 2017 6th International Symposium on*. IEEE, 2017.

[3] M. Sparing, A. Berger, F. Wall, V. Lux, S. Hameister, D. Berger, and L. Schultz. "Dynamics of rotating superconducting magnetic bearings in ring spinning". *IEEE Transactions on Applied Supercond.*, *26*(3) 2016: 1-4.

[4] S. Sivrioglu, S. Basaran, and A. Yildiz. "Multi surface HTS-PM levitation for a flywheelsystem," IEEE Transactions on Applied Superconductivity 26, no.4, 2016.

[5] Z. Yu, G. Zhang, Q. Qiu, L. Hu, B. Zhuang, and M. Qiu, "Analyses and tests of HTS bearing for flywheel energy system". *IEEE Transactions on Applied Superconductivity*, *24*(3), 1-5.

[6] S. Sivrioglu and S. Basaran. "A Dynamical Stiffness Evaluation Model for a Ring-Shaped Superconductor Magnetic Bearing System," *IEEE Transactions on Applied Superconductivity 25(4),* August 2015.

[7] S. Sakai, Q. Koichi, and O. Shunsuke. "Effect of the Magnetic Configuration on the Rotational Motion in the Attractive-Type HTS-Permanent Magnet Hybrid Bearing." *IEEE Transactions on Applied Superconductivity* 26.4 (2016): 1-4.

[8] A.J. Arsénio, M. V. Carvalho, C. Cardeira, P.J. Costa Branco, and R. Melício. "Conception of a YBCO superconducting ZFC magnetic bearing virtual prototype." *IEEE International Power Electronics and Motion Control Conference (PEMC*), pp. 12261230, IEEE, 2016.

[9] P.J. Costa Branco, and J.A. Dente. "Design and Experiment of a New Maglev Design Using Zero-Field-Cooled YBCO Superconductors." IEEE Transactions on Industrial Electronics, Vol. 59, No. 11, Nov. 2012

[10] J. Fernandes, I. Montes, R. Sousa, C. Cardeira, and P.J. Costa Branco. "Superconductor joule losses in a zero-field-cooled (ZFC) maglev vehicle." IEEE Transactions on Applied Supercond. 90 (2016): 1-7.

[11] A.J. Arsénio, M.V. Carvalho, C. Cardeira, R. Melício, and P.J. Costa Branco. "Experimental Setup and Efficiency Evaluation of Zero-Field-Cooled (ZFC) YBCO Magnetic Bearings." *IEEE Transactions on Applied Superconductivity 27*, no. 4 (2017): 1-5.

[12] A.J. Arsénio, M.V. Carvalho, C. Cardeira, P.J. Costa Branco, and R. Melício. "Viability of a frictionless bearing with Permanent Magnets and HTS bulks." *IEEE International Power Electronics and Motion Control Conference (PEMC)*, pp. 1231-1236, IEEE, 2016.

[13] J. Mais, "Spectrum Analysis: The Key Features of Analyzing Spectra." San Diego: SKF USA Inc.; May 2002.

[14] T. L. Bergman and F.P. Incropera. Fundamentals of heat transfer and mass transfer. John Wiley & Sons, 2011.

[15] M. V. Carvalho, A. J. Arsenio, C. Cardeira, P. J. C. Branco, and R. Melício. Levitating bearings using superconductor under smarts systems scope. In: Technological Innovation for Smart Systems, pages 390-397, May 2011.